RESEARCH PAPER

Influence of Thermal Residual Stresses on the Behaviour of Metal Matrix Composite Materials

Roberto Alonso González-Lezcano[1] · **José Manuel del Río-Campos[2,3]** · **Tamar Awad Parada[2,3]**

Abstract

In this article, numerical simulations are used to study the bonding of ceramic–metal interfaces as well as ceramic-reinforced metal matrix composites (MMCs). For the design of the geometrical model of the MMC, the reinforcement is considered to be discontinuous (MMCD) and it consists of particles in which their distribution is homogeneous within the composite material. As a consequence of the existence of residual stresses in the material, there will be higher compressive stresses in the reinforcement and higher differences of stress values between the matrix and the reinforcement than those found without them. The novelty of this research lies in the fact that through the knowledge of the stress states at a given distance from the interface, the manufacturing processes of the MMCs could actually be improved. After the simulations, it is observed that the reinforcement is compressed due to the difference between the two thermal expansion coefficients of the constituent materials. The matrix is also compressed in the incident zone longitudinal to the reinforcement and in the zone surrounding the fibre in the radial direction. However, the matrix is tensioned in the longitudinal direction parallel to the reinforcement and in the transverse direction around the particle.

1 Introduction

Ceramic–metal interfaces are playing an increasingly relevant role in various engineering areas, such as microelectronics, automotive, and the manufacture of metal matrix composites with a ceramic reinforcement (MMCs) (Yang et al. 2021; Zhao et al. 2021; Zhang et al. 2017). Bi-materials generally have very good characteristics for use in a wide range of high temperature applications, such as gas turbines, heat exchangers, or combustion chambers. In recent years, great efforts have been made to achieve better bonds between ceramic and metallic materials, as well as to design bonding processes valid for a wide range of industrial uses (Zhang et al. 2017) including cryogenic treatments (Hussain et al. 2017).

The addition of ceramic particles to a metal matrix increases the stiffness and mechanical strength of the material, while maintaining its isotropic behaviour, resulting in a combination of price and mechanical properties, making these metal matrix and ceramic reinforcement composites optimal materials for many industrial applications (Chen et al. 2020a; Hu et al. 2021).

A bi-material made up of the union of a ceramic material and a metallic material, when it cools down after its manufacturing process or when it undergoes a subsequent thermomechanical treatment, presents a field of residual stresses that originate in the difference between the respective moduli of elasticity and the coefficients of thermal expansion of both materials (Das et al. 2019; Kalaiselvan et al. 2021; Patil et al. 2020; Shankar et al. 2020;

✉ Roberto Alonso González-Lezcano
rgonzalezcano@ceu.es

José Manuel del Río-Campos
jmdrc.eps@ceu.es

Tamar Awad Parada
tawad@icai.comillas.edu

1 Escuela Politécnica Superior, Montepríncipe Campus de Boadilla del Monte, Universidad San Pablo-CEU, CEU Universities, 28040 Madrid, Spain

2 Department of Mechanical Engineering, Technical School of Engineering – ICAI, Comillas Pontifical University, Alberto Aguilera 25, 28015 Madrid, Spain

3 Product Design Department, University School of Design Innovation and Technology, ESNE, Av.de Alfonso XIII, 97, 28016 Madrid, Spain

González-Lezcano and Río Campos 2019). These residual stresses significantly influence the mechanical behaviour of the ceramic–metal interface and can cause deformations up to failure, affecting the integrity of the structure of which the ceramic–metal bond is a part (Balokhonov et al. 2021, 2022; Xiong et al. 2021).

Due to their industrial importance, bonding methods between ceramic and metallic materials have reached a high level of development (Zhang et al. 2015). However, there is still a need for further research into effective bonding techniques, a thorough understanding of the interface structure affecting both mechanical and thermal properties, control of the bonding mechanisms and evaluation of the residual stress distribution, the effect of which is very detrimental to the mechanical behaviour of the bimaterial (Zemlianov et al. 2020; Shokrieh 2014; Sidhu et al. 2015).

Although the interfaces between ceramic and metallic materials have been thoroughly investigated in the past (especially in some cases of ceramic-reinforced metal matrix composites or Cu-Ag brazing alloys), there is still little information on their thermomechanical properties, particularly in the case of non-oxide ceramic materials such as silicon nitride (Si_3N_4) (González-Lezcano et al. 2020; Wang et al. 2019; Liu et al. 2017; Shi et al. 2006; Ong et al. 2021). In actual application, many problems remain unsolved, including how to assess and compensate for the high residual stresses arising both during the cooling following the bonding process and after subsequent thermo-mechanical treatment (Wang et al. 2017).

The thermomechanical properties and thermal residual stresses of ceramic–metal interfaces, both from the bonding of the two materials and from the manufacture of metal matrix composites with ceramic reinforcement, can in many cases be evaluated by experimental tests (Magally et al. 2016). However, this is not always feasible, as such tests are often very complex or expensive. One way to solve this problem is to use numerical simulation methods, which allow fairly valid approximations of these parameters to be obtained without the need for experimental testing (Chen et al. 2020b; Kunčická et al. 2020). For this reason, numerical simulation methods have become very important due to the reduction in costs and development times of the execution processes (González-Lezcano and Río 2015).

Furthermore, the number of investigations presenting a comparison between results obtained by experimental and numerical measurements is scarce in the scientific literature. With optical residual stress measurement techniques (e.g. Raman microscopy, neutron diffraction, X-ray), it is possible to reach detailed approximation levels down to the grain size; however, there are few comparative studies of these experimental values with numerically obtained residual stress distributions at a mesoscopic level (Stanković et al. 2019; Kumar and Curtin 2007).

On the other hand, ceramic–metal interfaces in metal matrix composites with ceramic reinforcement have an additional disadvantage: their mechanical properties are influenced by a multitude of factors, such as different possible reinforcement geometries, different size distribution patterns, particle slenderness or reinforcement volume ratio, effects that have not been studied in depth either (Soleymani Shishvan and Asghari 2017).

Although there are other studies on the influence of the geometry of the reinforcement on the mechanical behaviour of materials for minimization of surface roughness and hole overcut or the effect of cutting parameters on surface finish, the novelty of our research work lies on the identification of the highest values of stress within the matrix-particle interface, so that it is remarkable to note it. Therefore, it is necessary to emphasize the importance of focusing on the decohesion of the reinforcement relating to its mechanical behaviour.

Consequently, there is still a need for a systematic study, both macroscopic and microscopic, of the generation of these types of stresses and for their characterization from a scientific point of view, a basic requirement for understanding the properties of bimaterials and the potential of their applications (Sackey and Smith 2009).

The origin of residual stresses of thermal origin at ceramic–metal interfaces lies in the difference between the coefficients of thermal expansion of the two materials (since the coefficient of thermal expansion of a ceramic material is usually lower than that of a metallic material), although it is also due to the difference between other properties, such as the modulus of elasticity (Sijo and Jayadevan 2016).

The appearance of residual stresses has a more pronounced effect on ceramic–metal interfaces involving Si_3N_4, due to the greater difference between the coefficients of thermal expansion of this ceramic material in relation to other ceramics for industrial use, particularly oxidic ceramics (Huang and Ali 2019). This high difference between the coefficients of thermal expansion generally leads to the breakdown of such interfaces. A comparison of the values of the thermal expansion coefficients for nickel (i.e. Ni) and silicon nitride is shown in Table 1.

For centuries, thermal residual stresses from the manufacturing process of many materials have been identified by both manufacturers and users. Ancient civilizations, for example, were already aware of thermal residual stresses in

Table 1 Values of the coefficient of thermal expansion

Material	Coefficient of thermal expansion $\times 10^6$ (K^{-1})
Si_3N_4	3,3
Ni	13,3

glass and mitigated them by heat treatment after the manufacturing process. Glass annealing, which dates back centuries, is one of the most widely recognized post-treatments for the control and attenuation of these internal stresses (Gigliotti 2016; Shin et al. 2007).

In most cases, the occurrence of residual stresses of thermal origin is usually associated with a decrease in mechanical strength and fatigue resistance, sometimes with separation of the material into sheets, distortion of shape, or even corrosion. Certain mechanical properties (such as yield strength and toughness) can be significantly affected by the presence, magnitude, or sign of residual stresses (Lezcano and Río 2017; Senthil et al. 2020). These effects are compounded by the structural anisotropy characteristics of the material in the case of a MMC, as well as its gradual composition in the case of functionally graded material (i.e. FGM) interfaces. It is therefore crucial for the integrity of such interfaces to know and control the thermal residual stress distribution resulting from their manufacture and further processing (Amirkhanlou et al. 2013).

In addition, the residual stress state is usually a dynamic process, as there are many stress relaxation processes occurring within the material, such as plastic deformations at the interface, slippage between the matrix and the reinforcement, material buckling, micro-cracking, or fibre buckling (Logesh and Bupesh Raja 2017; Wady et al. 2003). Although some of the relaxation processes can be activated even at room temperature, it is difficult to identify which relaxation process is active by simply measuring the existing stresses in the material, which implies an additional major disadvantage in the evaluation of the stresses.

Residual stresses have been qualified by several authors (Salvati and Korsunsky 2017; Fu et al. 2021; Everaerts et al. 2018) according to the length scale on which they act. Type I residual stresses, also called macroscopic, are referred to distances measured in millimetres and may be due to non-uniformity of the temperature field (Duhamel's theorem) or to different cooling rates within the material.

Residual stresses produced at the mesoscopic scale occur at a scale between 1 and 100 μm and are often referred to as Type II. Within these residual stresses are those produced by MMCs as an interaction between the reinforcement material and the matrix material, mainly due to the difference between the thermal expansion coefficients of the two materials. Finally, Type III residual stresses describe residual stresses existing at the atomic scale, such as those produced by accidental dislocations.

In ceramic–metal interfaces from joints, residual stresses of thermal origin are due to the manufacturing process, whether in the case of hot isostatic pressing, high temperature welding, or sputtering (Moreno et al. 2009). They are usually Type II when they are due to the difference in thermal expansion coefficients and Type I if they originate as a consequence of heterogeneity problems in the temperature distribution. In the case of ceramic–metal interfaces from a MMC, the residual stresses generated during the extrusion process are of particular interest and are also associated with these two types of stresses, as described below.

The aims of this article are:

- **Numerical modelling** of the cooling process during the fabrication of a ceramic–metal bond in order to evaluate the resulting residual stress distribution of thermal origin (at the macroscopic level) and including a ceramic–metal interface of similar chemical composition and constitutive laws to reality.
- **Model previous validation** by cross-checking its predictions with measurements made by optical methods (X-ray diffraction, from values provided by the Institute of Ceramics and Glass).
- **Numerical modelling of a bending test** performed on the bimaterial at mesoscopic level and comparison of these data with the same test performed on a ceramic monomaterial specimen, as well as comparison of the results with the superimposition of the stress fields predicted by the macroscopic model on the mesoscopic one.
- **Use of the models described above** to draw conclusions about the thermomechanical behaviour of the ceramic–metal interface at the joint and to predict which area of the joint is likely to initiate cracking, using stress criteria.

2 Methodology

In order to simulate a thermomechanical or physical problem, it is first necessary to model it geometrically. This representation must be as faithful as possible to reality so that the results obtained after the numerical calculation on these models are reliable.

In this article, numerical simulations are used to study the study of ceramic–metal interfaces from both metal–ceramic and metal–ceramic bondings and ceramic-reinforced metal matrix MMCs.

Two types of geometric models have been developed:

- The first type of models will be used to predict the residual stress distribution resulting from the cooling process of the material.
- The second type of models shall be used to apply mechanical situations where the residual stress state is superimposed on a stress state induced by mechanical stresses, such as bending or tensile stresses.

In order to study the residual stress field arising at the macroscopic level during the post-fabrication cooling of the ceramic–metal bond, two types of configuration have

been developed: a macroscopic and a mesoscopic model. The first, called model A-I (as shown in Fig. 1), consists of two parallel sheets (one metal and one ceramic). This model corresponds in dimensions and geometrical shape to a real specimen manufactured by the Hot Isostatic Pressing (HIP) process from which experimental data have been obtained and which will be compared with those obtained by simulation.

In order to study the behaviour of the ceramic–metal bond under the action of a bending stress, the other model mentioned above has been carried out, at a mesoscopic level (model A-II), on which the results of residual stresses obtained in model A-I will be transferred. This model A-II is shown in Fig. 2.

The reason for this second model is that it allows the bending test to be modelled much more accurately, so that the shear stress is applied directly to the ceramic–metal interface.

Using stress criteria, it will be possible to predict which zone of the specimen is likely to initiate a crack. These results for the bi-material model will be compared with those obtained by similar numerical simulations carried out with a model made exclusively of ceramic material (mono-material).

For the case of the ceramic–metal interface from the metal matrix and ceramic-reinforced MMC, two models have been considered: a macroscopic and a mesoscopic model.

For the design of the geometrical model of the MMC, the following assumptions have been taken into account:

(i)   The reinforcement has been considered to be of discontinuous type (MMCD) and formed by particles.
(ii) The particle distribution has been assumed to be homogeneous within the composite material.

The microstructure of a particle-reinforced composite material can become very complicated depending on the particle type, size, geometry, and its distribution in the matrix (Ge et al. 2019; Han et al. 2020; Tian et al. 2020; Du
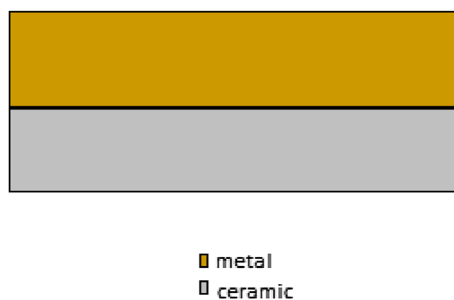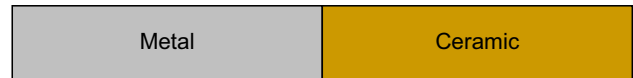
Fig. 2 Type mesoscopic model A-II

et al. 2018). In the thermomechanical process, therefore, many more parameters are involved than in the case of bonding. The probability of breakage of the ceramic particles, for example, which depends on different geometries that the particles may have, becomes a relevant factor in the results (Suo et al. 2021; Chen et al. 2021; Sun et al. 2020; Aman et al. 2011; Uzi and Levy 2021; González Lezcano et al. 2003; Tavares et al. 2020). Two working hypotheses have been considered for a study that is as close to reality as possible.

The first hypothesis consists of studying a composite material formed by a metallic matrix and a reinforcement of ceramic particles, all of them of a medium size and uniformly distributed in the material. In the second scenario, the matrix is also considered to be reinforced by a uniform distribution of particles, but in this case of three different sizes.

For the study of both models, the material has been represented as a spatial grid of elements, resembling a grid of 27 distributed particles as shown in Fig. 3.

Designing an accurate model is an arduous task, so geometrical simplifications are often made on the condition that the final results are close to the real ones. Although the particles are spherical or ellipsoidal, portions of the particle have been represented in order to simplify the model. Each unit cell will consist of a piece of matrix and a reinforcement particle at its centre.

The type of thermomechanical problem encountered in the study of ceramic–metal interfaces is clearly nonlinear, which makes it necessary to resort to specific techniques for solving nonlinear problems. Both linear and most of the nonlinear problems—which are more complex and considerably more time-consuming than the former—can be solved
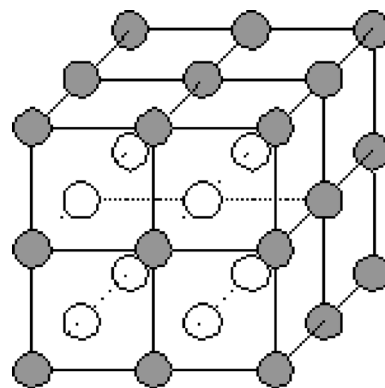
Fig. 1. Macroscopic model type A-I

Fig. 3 Schematic of the spatial distribution of particles in a MMC

by using numerical simulation based on the finite element method, described below.

Solving elasto-plasticity problems by the finite element method requires the use of nonlinear problem-solving techniques, as opposed to the linear techniques used to solve elasticity problems. Once the problem to be studied is known, during the pre-processing phase, a numerical model is built to represent it as accurately as possible.

For the numerical analysis carried out in this article, the commercial program Abaqus has been used. Abaqus is a general purpose finite element program that implements large analysis capabilities, including the possibility of defining specific constitutive equations by means of user subroutines.

Other studies on the influence of stirrer blade design on the microstructure and mechanical properties of a novel aluminium metal matrix composite or the production of metal matrix composites through stir casting as well as the compressive response of aluminium metal matrix composites have been taken into consideration (Krishnan et al. 2021; Ramanathan et al. 2019; Arunachalam and Krishnan 2021).

When transferring this cell to a macroscopic model, the model has been represented as a portion of the previous one, according to longitudinal and transverse cuts. Thus, for the macroscopic model (which has been denoted B-I, as shown in Fig. 4) and in order to calculate the residual stress distribution, the particle has been modelled exclusively in a cylindrical shape.

Obviously, different geometries could also have been considered when representing this macroscopic model of the MMCD; but, for reasons of simplification, in this case we have chosen to use this solution and include the other alternatives in the mesoscopic model.
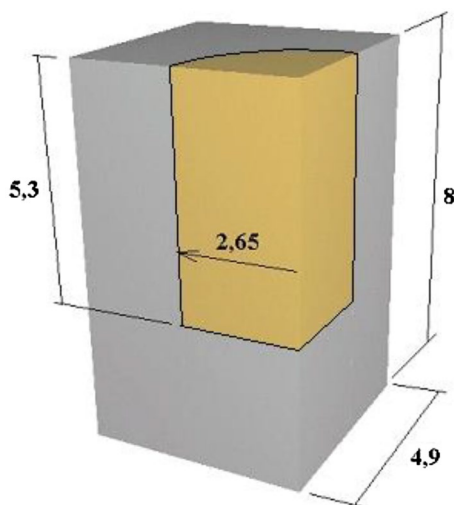
Due to the wide variety of shapes that the constituent reinforcements of a MMC can have (as described above), different geometric models have been used to represent each type of reinforcement by translating the macroscopic model into a mesoscopic model.

Thus, as we are dealing with axially symmetrical cells, the study will be carried out on the basis of the two-dimensional representation of the fourth part of each unit cell, so that the initial model is obtained again after a 360º revolution of the mesh.

Reinforcement particles often take irregular shapes, so in order to represent different types that can be found in reality as accurately as possible, four different kinds of reinforcements have been used: cylindrical reinforcements with the same diameter as the height, cylindrical reinforcements where the height of the particle is greater than its diameter, as well as spherical and ellipsoidal reinforcements.

The reason these models have been chosen is to try to represent the broad spectrum of particle reinforcement types that can be found in reality. Thus, spheres are suitable for reinforcement models of equal geometry or rounded shape, while cylinders are a good approximation for irregularly shaped reinforcements with sharp corners.

A cylindrical particle has a higher number of stress concentration points compared to spherical or ellipsoidal particles, which have smoother shapes. Another important factor to take into account is the influence of the relationship between the longitudinal and transverse dimensions of the particles on the material properties, so it is interesting to compare cylindrical particles in which the diameter is equal to the height and cylindrical particles in which the height is greater than the diameter. Finally, it is also interesting to carry out studies of the distribution of reinforcement according to different particle sizes, as will be discussed later.

The unit cell model simulates the composite material represented by a single reinforcement within the matrix, as shown in Fig. 5, so that the geometrical relationships of the constituents are fulfilled. In order to achieve an approximation as close as possible to reality, four different types of particle geometries have been considered, namely cylindrical of equal diameter and height (hereafter referred to simply as cylindrical), cylindrical of height greater than the diameter (hereafter referred to as elongated cylindrical, spherical, and ellipsoidal). For this purpose, it is important to establish the average particle dimensions, the relative distances between the particles, and the volume fraction of the reinforcement.

On these models, referred to as B-II, the tensile stresses mentioned above shall be applied superimposed on the residual stress distribution obtained.
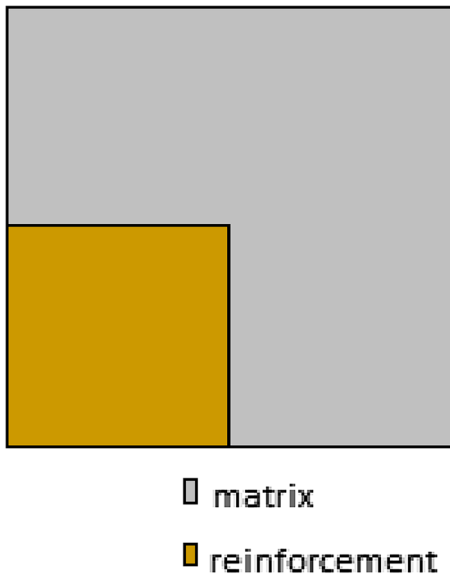

Fig. 4 Macroscopic model type B-I

matrix

reinforcement

Fig. 5. Type B-II mesoscopic model (unit cell model) for a cylindrical particle

Fig. 6. Instron universal testing machine, model 8516 with a maximum load of 100 KN used to perform either tensile tests or compressive tests

2.1 Application of Loads and Boundary Conditions

The numerical models include the application of loads and boundary conditions in order to simulate the relevant mechanical tests that induce stress fields superimposed on the previously calculated residual stress distributions. In this way, bending and tensile tests similar to those obtained experimentally have been simulated using a universal testing machine as shown in Fig. 6.

From the results obtained numerically, conclusions will be drawn on the influence of the residual stress state on the mechanical behaviour of the ceramic–metal interface and on the initiation of cracks in the material, in comparison

with other mono-material specimens. The boundary conditions are:

- Two supports with restricted movement in the vertical axis.
- An additional constraint on the horizontal movement of the lower centre point of the specimen to avoid rigid solid movements.

Analyses of the specimen have been carried out in different situations in terms of the load application zone, from a point application to a distribution in a 1 mm zone. Obviously, the application of the load in a narrow area (as is the extreme case of point application) causes very high stresses to appear and constitutes a singularity of the stress field which does not correspond to reality; since the load is inevitably applied over an area whose dimension is at least the width of the application instrument.

Therefore, a uniformly distributed load in a region of approximately 1 mm has been modelled to avoid the effects of high local stresses that could be produced by a point load. In any case, the stress values obtained in the vicinity of the loading zone will not be representative.

In the case of the MMC, the initial conditions or constraints that define the model have been defined. As it is an axisymmetric model, the mesh that defines the unit cell representative of the material will be axially symmetric. Thus, the axes $z = 0$ and $r = 0$ have the following symmetry relations:

The axis (U1) $z = 0$ (lower side of the mesh) presents a symmetry defined by the program as YSYMM which imposes the conditions $U1 = UR2 = UR3 = 0$. In the case of broken particle, this condition has only been imposed in the area of the axis that corresponds to the material of the matrix, since, as the particle is fractured, it no longer presents symmetry.

The axis (U2) $r = 0$ (left side of the mesh) presents a symmetry defined by the program as XSYMM which imposes the conditions $U2 = UR1 = UR3 = 0$. On the right side of the mesh ($r = R$), the condition $U2 = 0$ has been imposed, to avoid displacement in this direction and thus simulate the existence of the rest of the material (which is the real cause of this impediment).

The loads have been applied on the upper side of the mesh ($z = L$), so that the model can be subjected to two different types of stresses: the application of a stress distribution, with which the finite element program calculates the displacements of each element, or the imposition of a specific displacement, which in this case makes it possible to obtain the value of the stress distribution that causes the deformation.

The latter has been the option chosen in this article, whereby the nodes of the upper edge have been subjected

to a series of displacements corresponding to different values of deformation, in order to obtain a sufficient number of points of the stress distribution with which to construct the stress–strain curve of the MMC subjected to the prior residual stress field.

3 Results

For the three-dimensional specimen, the nomenclature convention established for both the experimental measurements and the numerical calculation has consisted of naming as *axis 2* the axis corresponding to the axial direction, i.e. perpendicular to the interface, while *axis 1* has been chosen to name the radial direction, parallel to the interface. In Fig. 7, the section of the three-dimensional specimen is represented by the vertical plane passing through its centre and parallel to its faces of greater area, which corresponds to the macroscopic model type A-I described in 4.5, including the naming conventions relating to *axis 2* (vertical) and *axis 1* (horizontal). In addition, comparisons between numerical and experimental data have been made along two different measurement lines: LA, which passes through the middle of the lateral face of the three-dimensional specimen, and LB, which passes through the centre of the specimen. In both cases, the variable λ used was the distance to the interface when moving towards the inside of the ceramic part.

In reality, the residual stress has not been measured by X-ray diffraction, but is obtained by measuring the residual deformation caused by the cooling process of the material. The measurement of these residual strains by X-ray diffraction techniques is done by observing the variation in the inter-plane distance of the crystal lattice caused by the residual tensile or compressive stresses, as individual grains contract or expand at the microscopic level as a consequence of these stresses.

This variation can be detected from the change in the tilt angle of the incident beam. Using the Bragg equation, the longitudinal strain (ε) is defined as the relative change in the actual distance (d) between two lattice planes under residual stresses with res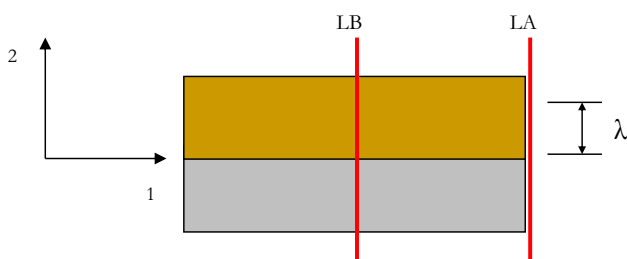pect to the initial distance (d_o) that existed between the same planes when they were free of residual stresses. In turn, this deformation can be related to the increase in the incident beam tilt angle by the equation:

$$\varepsilon = \frac{d - d_0}{d_0} = -\cot\theta \times (\Delta\theta)$$

Figure 8 shows the diffraction process whereby the incident beam is diffracted by changing the angle of inclination. As the measurement window has a total width of 2 mm with respect to its centre, for the case of measurements along the LA line the error in the experimental measurement has been estimated to be around ± 1 mm, and therefore, in some cases it has been necessary to make successive approximations in the numerical calculations along axis 1 (at 0 mm from the centre, at -0.5 mm, -1 mm and up to -1.5 mm) to find the closest comparison between the two values.

This experimental error margin is not so important for the values obtained along the LB line, because it is easier to fix the measurement window in the centre of the specimen than at its end; therefore, as will be seen below, no successive approximations have been made for the case of the LB line.

Both residual stress and residual strain results have been obtained from the numerical model and compared with the data obtained by X-ray diffraction. As can be seen in the corresponding figures, the experimental data and the FEM calculations show, in general, an agreement for the axial component (axis 2) of the LA strain. For the radial component of the strain (axis 1) in LA, although the approximation is not as accurate, the values obtained can also be considered equally admissible, as in the case of LB.

In view of the approximations obtained by numerical simulation, the numerical model chosen in this article has been validated.

3.1 Analysis of Deformational Behaviour

Figures 9, 10, 11, 12 show the axial and radial strain values for the LA and LB lines as the observer moves away from the interface in the direction of axis 2. The numerical values are shown together with those obtained by X-ray diffraction (XRD). Note that in some cases the distance chosen in the numerical simulation has been adjusted to the experimental
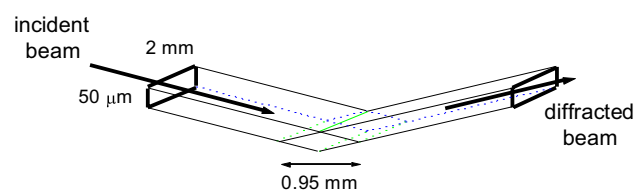

Fig. 7. Agreement of axes and measuring lines for numerical calculation and experimental measurement

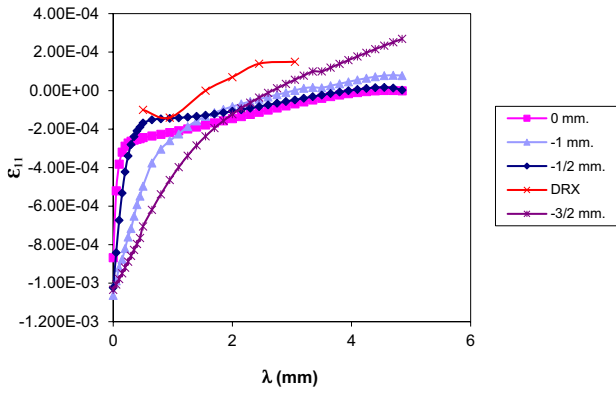**Fig. 8.** Change in incident beam angle and value of the measurement window

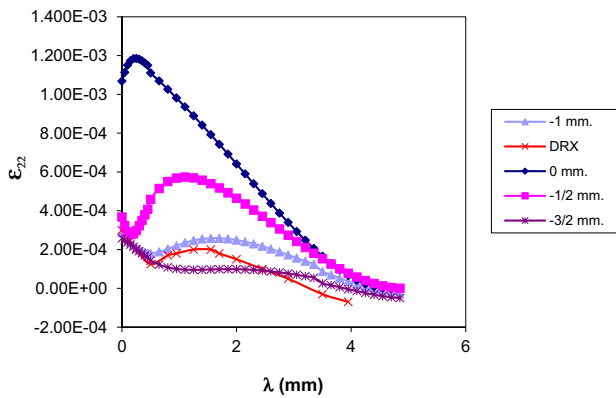**Fig. 9.** Radial strain versus distance λ to the interface along different parallels to LA

Fig. 10. Axial strain versus distance λ to the interface along different parallels to LA
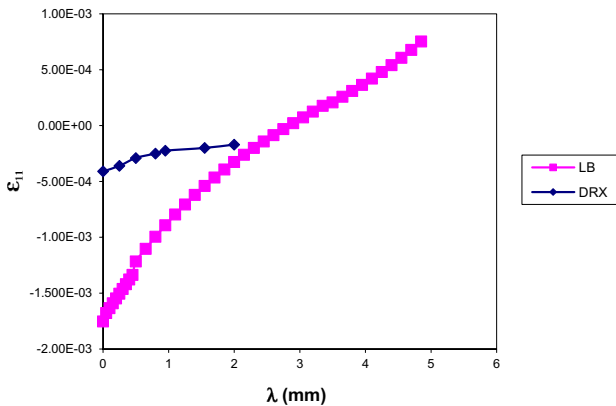

Fig. 11. Radial deformation versus distance λ to the interface along the LB line
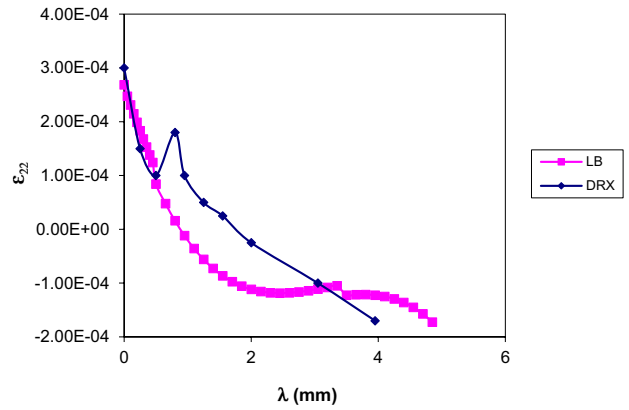

Fig. 12. Axial deformation versus distance λ to the interface along line LB

measurement on a parallel to LA towards the inside of the specimen at 0.5 mm, and so on.

Radial deformation has been denoted ε_{11} and axial deformation ε_{22}, in order to differentiate them from angular deformations resulting from tangential stresses (and which in Abaqus are usually represented by ε_{12} instead of γ).

As can be seen in the figures, the ordinate represents the measured residual strain and the abscissa the distance λ to the interface along the lines LA or LB.

In the case of the LA line, it can be seen that both in the radial and axial directions the experimental measurement was taken at a distance of between 1 and 1.5 mm from the end of the specimen, the value obtained in axis 2 being very close in both sign and order of magnitude (note that no radial values below 0.5 mm were taken).

For the case of the LB line, the values in the radial direction are less approximate (no experimental values were obtained at more than 2 mm from the interface), being the axial values very similar except for the peak obtained at 1 mm from the interface, which has not been observed in the numerical simulation and could be an outlier of the measurements.

A deformation analysis shows that the radial deformation can reach shortening values of up to 0.11% at the interface when the measurement is taken on the parallel to the LA drawn 1 mm from the end of the specimen. A progressive decrease in this value is also observed until it cancels out (at about 1.5 mm from the interface according to the XRD and at about 3 mm from the interface according to the numerical data if the measurement is taken parallel to the LA drawn at 1.5 mm from the end of the specimen). From this point on, the deformations become positive until reaching elongation values of up to 0.03%. As for the LB measurements, the trend of the curves is similar and the sign of the deformations is the same, although there is a greater difference between the experimental data, which show shortenings of
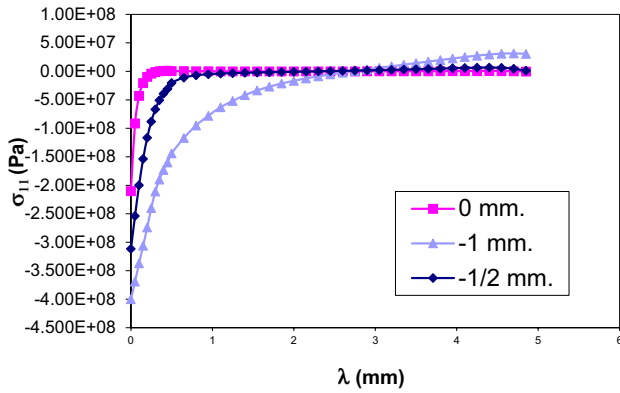
measurement distance, as mentioned above. Thus, the curve at 0 mm corresponds to the LA line at the exact end of the specimen. The curve relative to -0.5 mm corresponds to the

Fig. 13. Radial stress versus distance λ to the interface along different parallels to LA

Fig. 14. Axial stress versus distance λ to the interface along different parallels to different parallels to LA

0.05% at the interface, and the numerical data, which show shortenings of up to 0.18% in the same area.

For the axial deformations along the LA, it is observed that the numerical results reproduce with high fidelity the data obtained experimentally for a straight line parallel to the LA at a distance of 1 mm; a maximum of the deformation is observed at approximately 1.5 mm from the interface whose value corresponds, in both cases, to an elongation of 0.2%. The change of sign of the deformation from positive to negative at about 4 mm from the interface is also observed, both for the experimental and numerical values.

As for the measurements along the LB line, the values at the interface—elongations of 0.03%—coincide in both cases. In the numerical results, however, the maximum at 0.8 mm of the interface that appears for the experimental data is not observed, while there is the same change in the sign of the deformation between 1 and 2 mm approximately.

3.2 Analysis of Stress Behaviour

As mentioned in the previous section, although the residual stresses have not been evaluated by X-ray diffraction, they have been estimated by numerical calculation. Figures 13, 14, 15, 16 show the axial and radial stress values for the LA and LB lines as the observer moves away from the interface in the direction of axis 2, in the same way as was done for the residual strain. In this case, the numerical values have been exposed alone, since there are no data obtained by X-ray diffraction. Note that, in the same cases as for the deformation, the values have also been adjusted to the final measurement distance approximating the experimental one, in order to observe the evolution of the data. Therefore, as in the previous case, the curve at 0 mm corresponds to the LA line at the exact end of the specimen. The curve relative to − 0.5 mm corresponds to the measurement on a parallel to LA towards the inside of the specimen at 0.5 mm and so on.
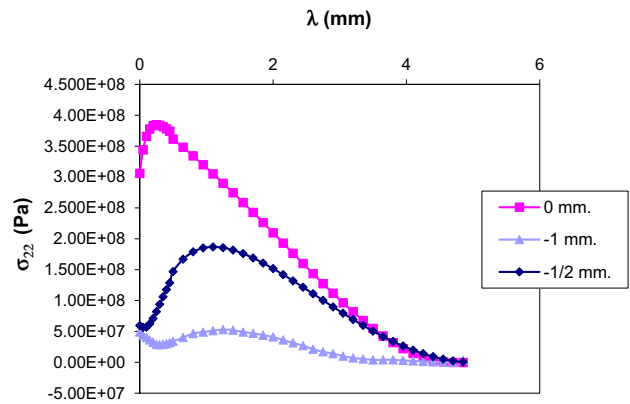

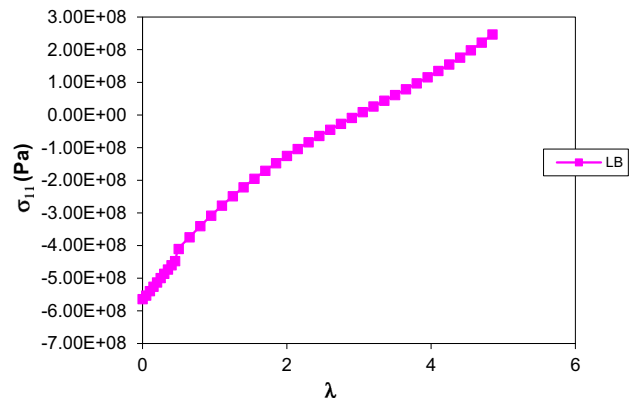**Fig. 15.** Radial stress versus distance λ to the interface along line LB
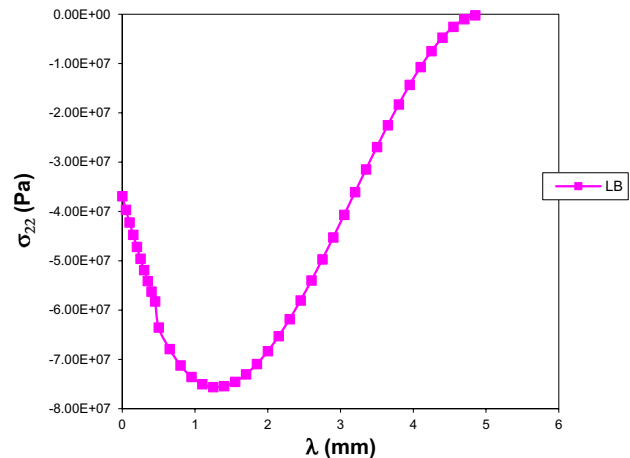

Fig. 16. Axial stress versus distance λ to the interface along line LB

Radial strain has been denoted as σ_{11} and axial strain as σ_{22}, in order to differentiate them from shear stresses (which in Abaqus are usually represented by σ_{12} instead of τ).

In the case of the LA line, it is observed that in the radial direction the stress is compressive for almost the entire specimen, with its maximum value located at the interface itself and with a value of between 200 and 400 MPa. At a distance of 3 mm from the interface, the radial stress practically cancels out or takes on tensile values of a lower order of magnitude. In contrast, in the case of axial tension, the maximum tensile values are not reached at the interface itself but at a distance of 0.3–1 mm from it, the highest value being approximately equal to 380 MPa.

For the LB line, the radial stress changes sign at 3 mm from the interface, going from compressive values (with a maximum of 560 MPa at the interface) to tensile values (with a maximum of 250 MPa) practically proportionally to the distance from the interface. In the case of axial tension, although the whole specimen is subjected to compression, the minimum value (75 MPa) is not obtained at the interface, but at 1.3 mm from it. This is the only stress in which a certain difference is observed compared to the evolution experienced by the corresponding deformation, in which, in addition, an experimental maximum was observed at a distance of approximately 1 mm.

If a stress analysis is carried out, it is observed that the radial stresses are at their maximum in the interface zone, both for the LB line and for the LA line and its parallels, obtaining compressive values in all cases. On the other hand, in all cases a change in the sign of the radial stress has been observed, which takes place at 3 mm from the interface, from which tensile values of a lower order of magnitude are obtained.

For the axial stresses, the measurements taken near the ends of the specimen give tensile values, whereas, as these measurements move towards the central area, the values are compressive. In both cases, the maximum values are not obtained at the interface, but at a certain distance from it, specifically at about 1 mm from it, as mentioned above. Anyway, Figs. 9, 10, 11, 12, 13, 14, 15, 16 allow us to conclude that the points at which the stress, either radial or axial, finds its maximum values.

As can be seen from the graphs, although in most cases the signs of the stresses and strains coincide, in some cases the sign of the stresses and strains do not coincide, which has been attributed to the effects of superimposition of strains due to the Poisson effect.

3.3 Results Obtained in the Mesoscopic Model

For the mesoscopic model A-II, and in order to make a comparison between results, two types of bending tests have been carried out. The first one, for a monomaterial specimen made entirely of ceramic, and the second, for a ceramic–metal bi-material specimen to which the residual stress field calculated in the previous section has been superimposed. In order to corroborate them, the residual stress values obtained have been compared with those obtained in the A-I model along the LA line.

3.4 Model of the Ceramic Test Tube

In order to validate the all-ceramic specimen model, a comparative study of the values obtained through the simplified calculation described above and those obtained through simulation with the Abaqus software has been carried out.

Subsequently, this model will also be used to obtain conclusions by comparing the numerical results obtained for this specimen with those calculated for the ceramic–metal specimen, in order to evaluate the influence that the replacement of the metal part of the bar by ceramic material has on the stress–strain behaviour of the same.

The numerical simulation has been carried out for a load of 2.5E5 N, a load that in the case of the single-material specimen causes stresses lower than the elastic limit of the ceramic material, so that the specimen will be in the elastic regime in its entirety.

Table 2 compares the calculated values and those obtained by numerical simulation using the ceramic specimen model (always within the elastic regime of the specimen).

For the A-II models, the same axes convention has been respected as for the A-I models, with axis 1 being horizontal and axis 2 vertical, although in this case the new axes are perpendicular to the previous ones.

Figures 17, 18, 19, 20, 21, 22, 23 show the stress distributions in the horizontal axis (S_{11}), shear stresses (S_{12}), maximum principal stress, displacements in the vertical direction (u_2), and longitudinal strains in both axes (E_{11} and E_{22}) for the all-ceramic specimen. The values of both stress and strain distribution are shown according to the colours specified in the table.

In view of these data, this model can be validated by comparison with the simplified calculations, since both the stresses and displacements obtained are quite close to reality in the simplified elastic case.

Table 2 Comparison of values obtained by simplified calculation and numerical simulation for the case of the ceramic specimen

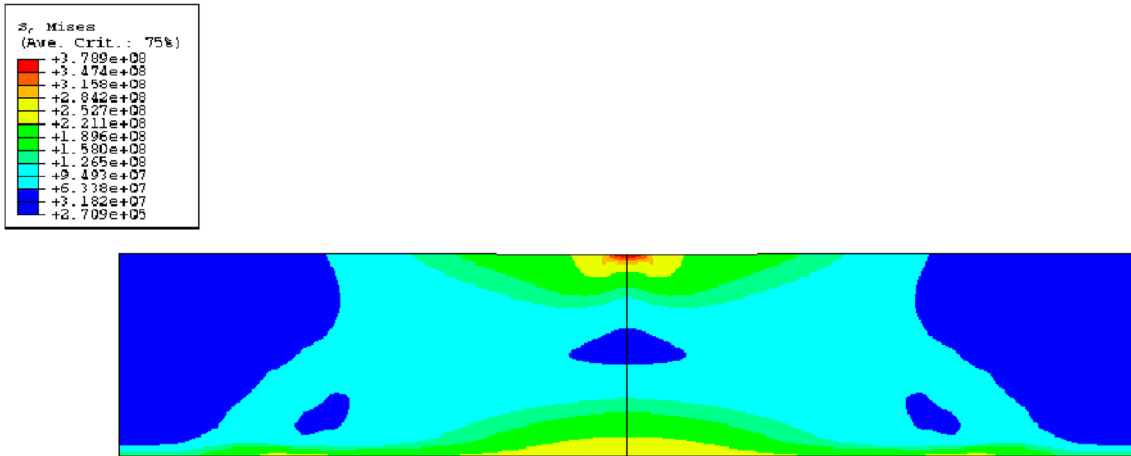| Parameter	Simplified calculation	Model
Flecha	0,014 mm	0,014 mm
σ_x	330 MPa	280 MPa
τ	6,25 MPa	6 MPa

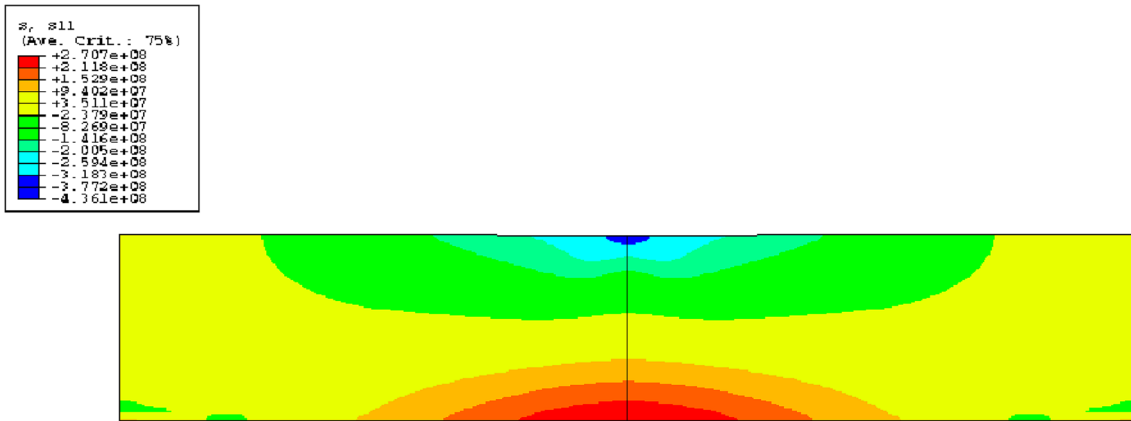**Fig. 17.** von Mises stress distribution for the all-ceramic specimen

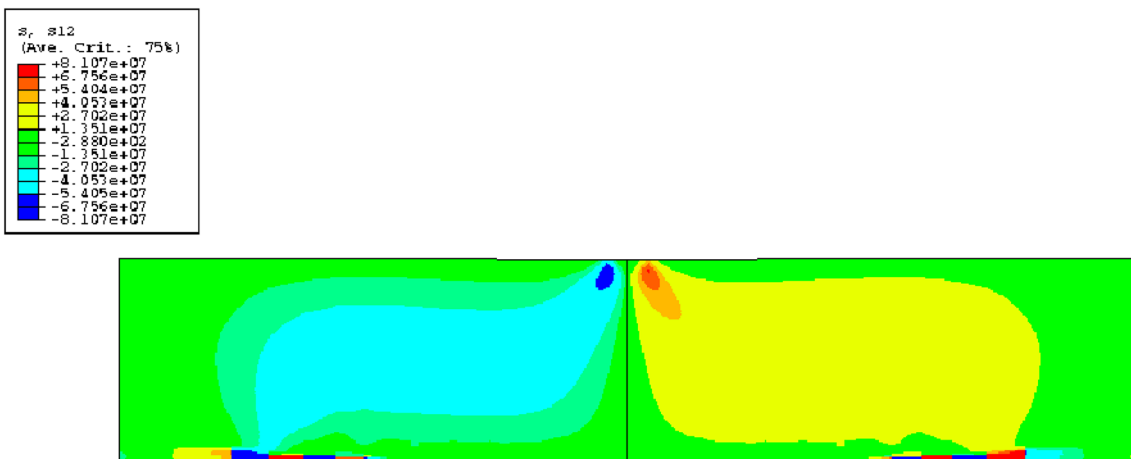**Fig. 18.** Stress distribution in the horizontal direction for the all-ceramic specimen

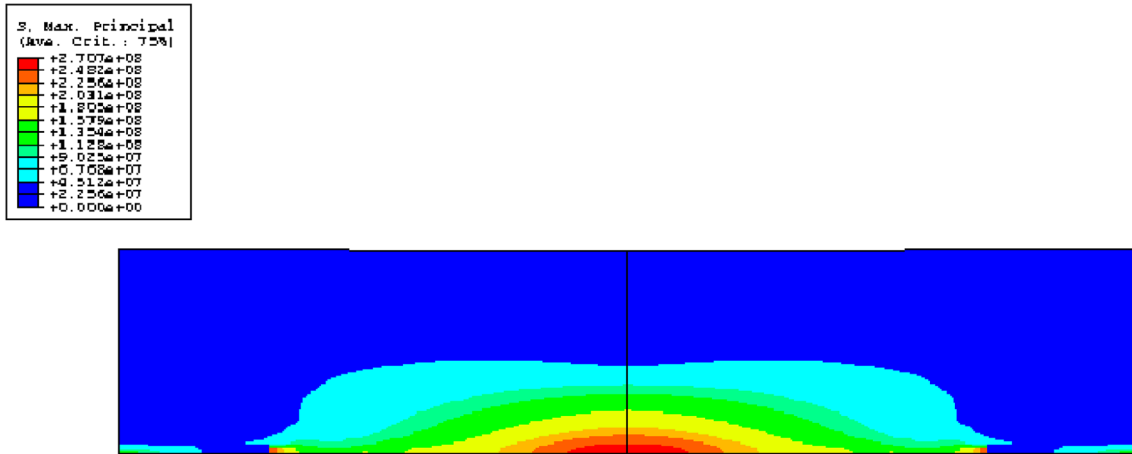**Fig. 19.** Shear stress distribution for the all-ceramic specimen

Fig. 20. Maximum principal stress distribution for the all-ceramic specimen
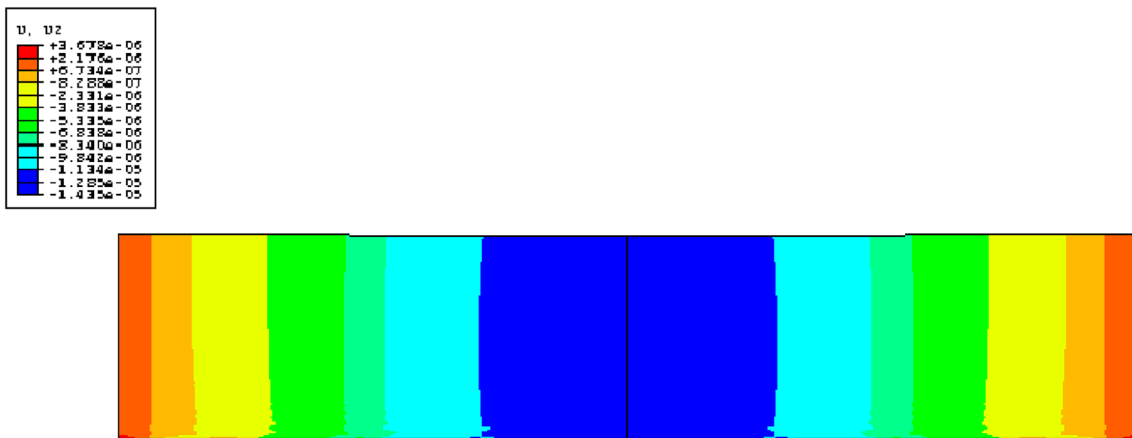

Fig. 21. Displacement distribution in the vertical direction for the all-ceramic specimen
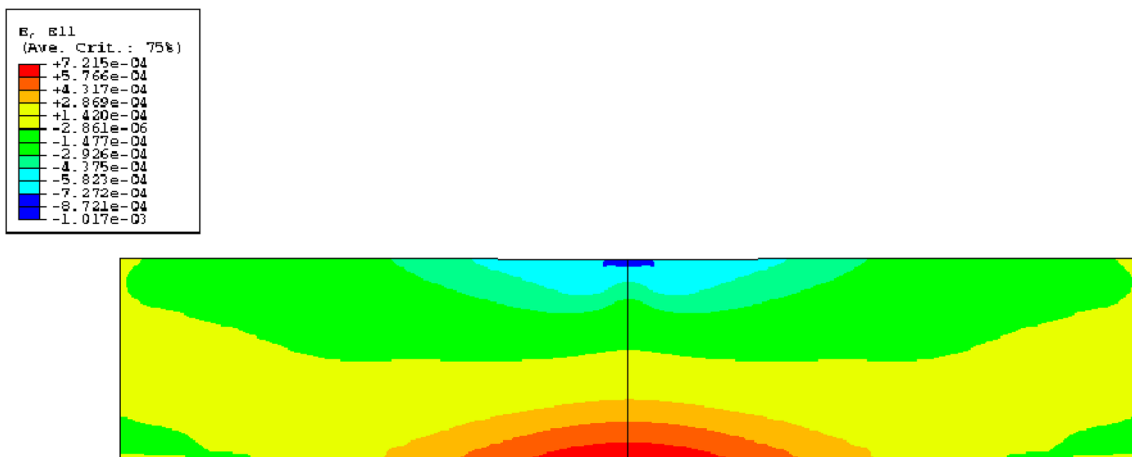

Fig. 22. Longitudinal strain distribution in the horizontal direction for the all-ceramic specimen
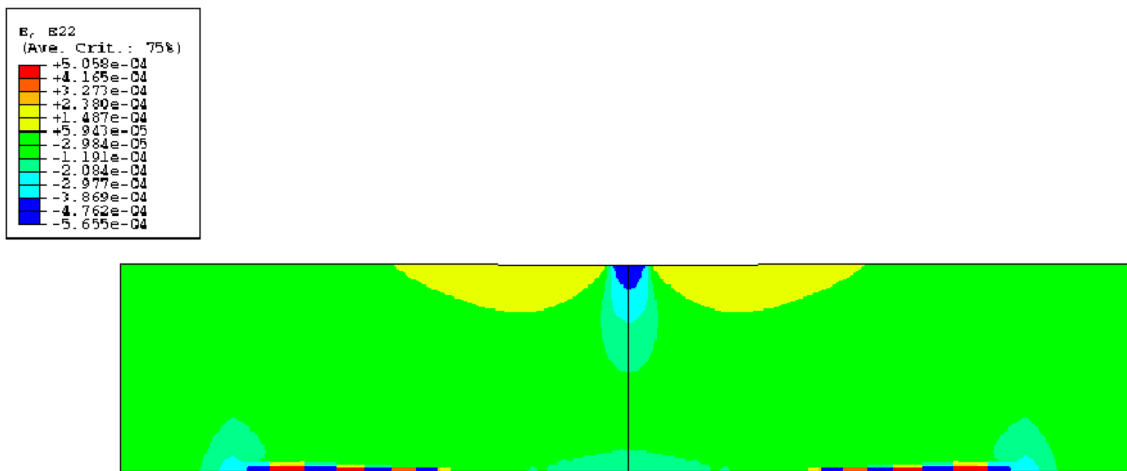
Fig. 23 Longitudinal strain distribution in the vertical direction for the all-ceramic specimen
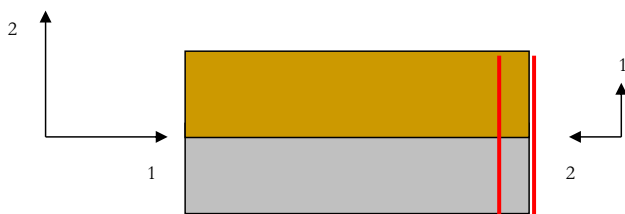

Fig. 24. Comparison between the axes considered at macro- and mesoscopic level

3.5 Model of the Ceramic–Metal Test Tube

Figures 25, 26, 27 show the equivalent stress distributions, stresses in the horizontal axis (S_1), shear stresses (S_{12}) for the ceramic–metal specimen. In this case, the simplified calculation cannot be used due to the difference in properties between ceramic and metal. In all figures, the metal region is shown on the left and the ceramic part on the right. Note that as a consequence of the change of model, although axis 1 is still considered horizontal and axis 2 vertical, the axis considered as 1 (radial) in the macroscopic model A-I becomes axial in the mesoscopic model, while the axis considered as 2 (axial) in the macroscopic model is in this case radial. Figure 24 shows this equivalence more accurately. The red lines indicate the section corresponding to the comparison with the mesoscopic model.

The mesoscopic model type A-II has been applied a cooling line similar to that of the macroscopic model, descending from an initial temperature of 1150 °C at a rate of 2°C/min and prior to the application of the bending load. These values of temperature and speed are the same that have been applied to the real macroscopic specimen manufactured by the HIP process, so they fit with great accuracy to the real
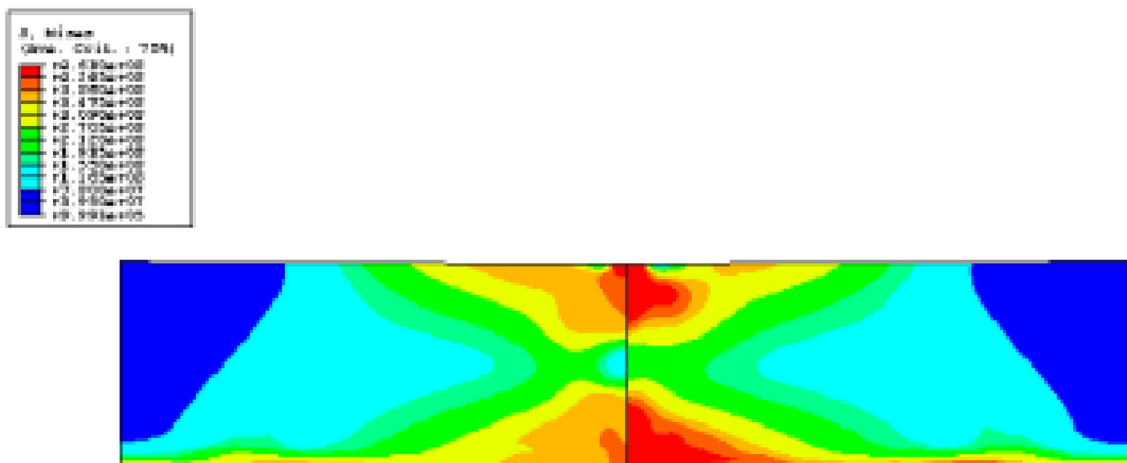

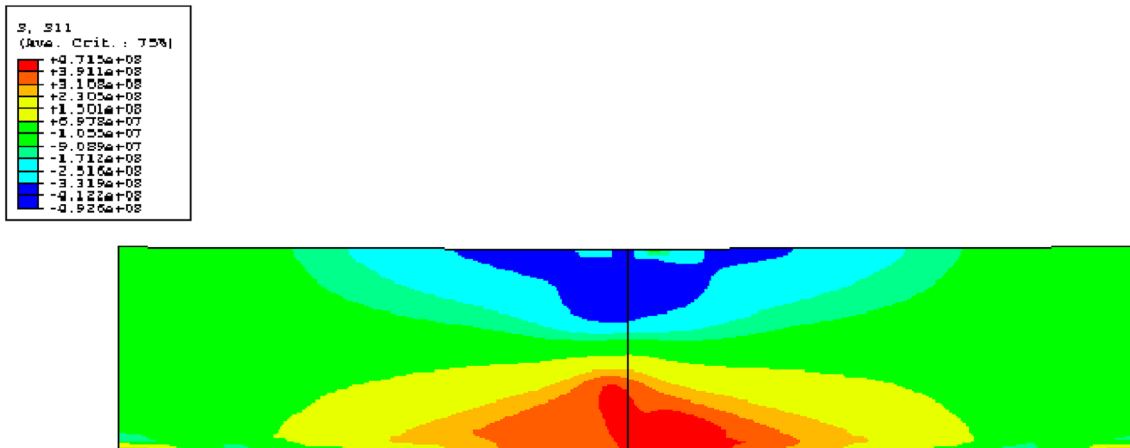**Fig. 25.** von Mises stress distribution for ceramic–metal specimen

Fig. 26. Stress distribution in the horizontal direction for the ceramic–metal specimen
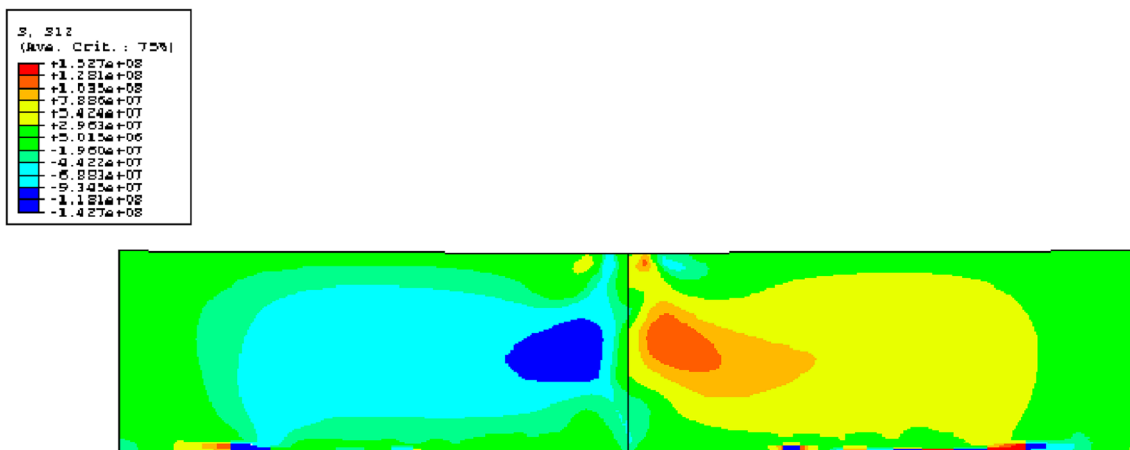

Fig. 27. Shear stress distribution for the ceramic–metal specimen.

manufacturing process if we had really manufactured a specimen of these dimensions.

3.6 Ceramic–Metal Interfaces in Mmc Residual Stresses Obtained After Cooling for a Single Unit Cell

In this case, the axial direction is called the *z*-axis, the radial direction the *x*-axis, and the tangential direction to the concentric circles on the *y*-axis.

After the cooling process of the MMC with metal matrix and ceramic reinforcement, it is observed that concentrated residual stresses appear, especially in the interface area.

As can be seen from Fig. 28, it can be observed that, in the case of axial tension, the reinforcement is subjected to compressive stresses of up to 600 MPa in the zone of the sharp edge. However, the matrix is subjected to compressive axial stresses in the zone close to the interface and under the base of the reinforcement—where the volume of matrix without reinforcement is smaller—which can reach up to 100 MPa in the live edge, while, for the rest of the matrix, the axial stresses progressively change sign until they become tensile, being in all cases these values of a lower order of magnitude.

For the case of the stresses perpendicular to the previous one, the entire ceramic reinforcement is subjected to compressive stresses, both in the x and y directions, while again in the matrix, compressive and tensile stresses are found depending on the area studied.

Figure 29 shows the example of the equivalent or von Mises stress distribution, where it can be seen that the highest values are, as expected, in the interface zone.

On the other hand, in the y-direction the matrix is almost entirely tensioned, reaching the highest values in

Fig. 28. Residual stress distribution in the axial direction for matrix and reinforcement
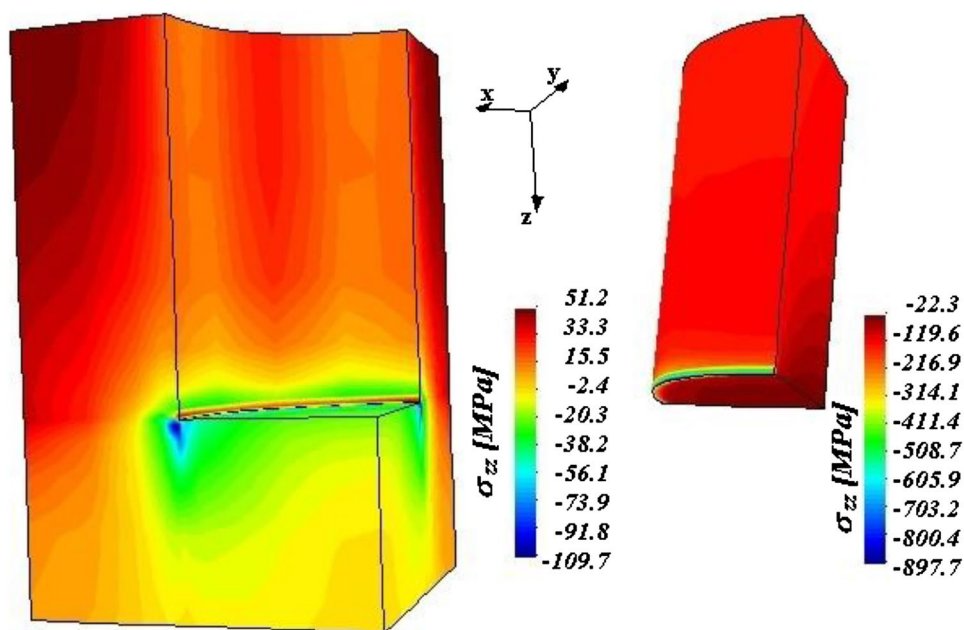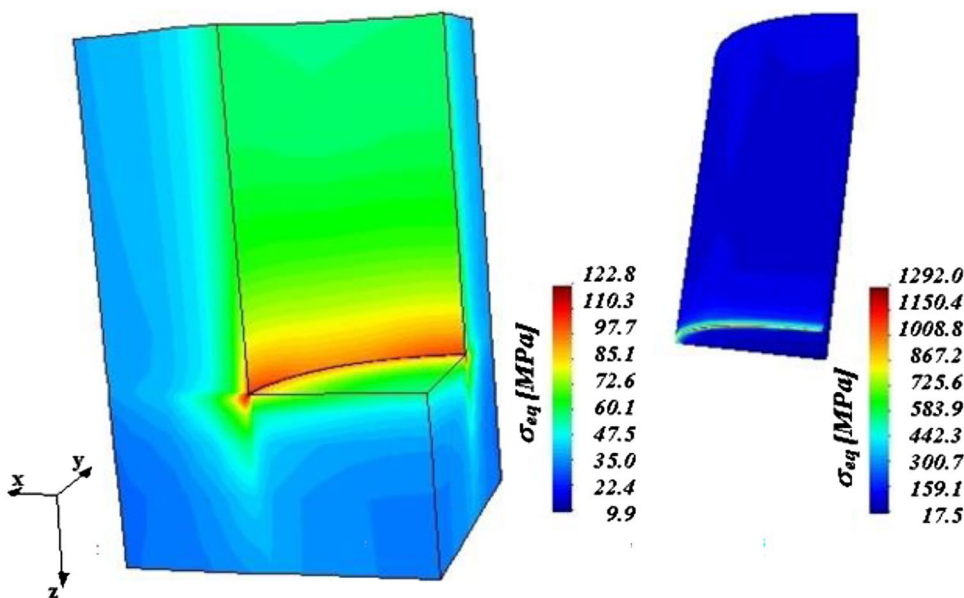

Fig. 29. von Mises stress distribution for matrix and reinforcement

the area where there is more matrix volume. In the region surrounding the reinforcement in the upper right-hand corner of the model, compressive residual stresses of up to 40 MPa are produced, stresses that become lower as the distance to the interface increases. In the opposite area of the matrix (upper left corner of the model), tensile values are reached, with higher values (up to 50 MPa) as the distance to the reinforcement increases. The radial stresses in the x-direction are equal to the *y*-direction but of opposite sign.

The above results are summarized in Fig. 30, where the direction of the stresses in the MMC after cooling can be

seen. As can be seen, the ceramic reinforcement is fully compressed in all directions.

4 Conclusions

4.1 On the Quality of the Models Used

In view of the results obtained, both macroscopic A-I and mesoscopic A-II models have been validated, being the degree of contrast of very good quality. It is therefore concluded that both models are validated for the analysis of the
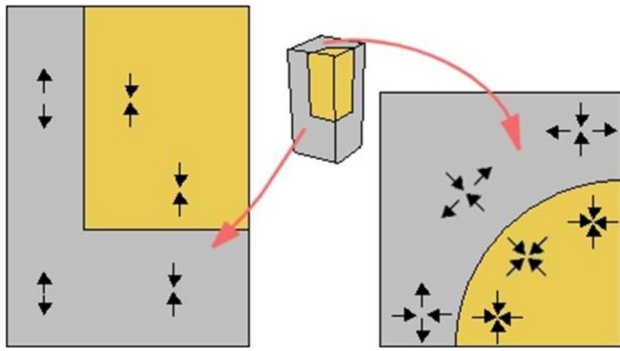
Fig. 30. Signs obtained for residual stresses after cooling of the macroscopic B-type model

Table 3 Comparative values between metal, ceramic, and ceramic–metal specimens

Model		σ_1 (MPa)
Ceramic	Monomaterial	280
	Bimaterial	470
Metal	Monomaterial	280
	Bimaterial	400

stress and deformation behaviour of ceramic–metal joints as a consequence of the residual stress state obtained during the cooling process.

X-ray diffraction combined with FEM analysis has proved to be a very useful tool for the study of the residual stress distribution resulting from the cooling of a ceramic–metal interface.

The importance of numerical simulation to approximate the macroscopic residual stress distribution in a MMC during its cooling process has been appreciated. The use of the B-II unit cell models has been very useful for obtaining results due to their good approximation to reality.

4.2 On the A-II Mesoscopic Model

Generally speaking, the stress field in the ceramic zone reaches higher values than in the metallic zone, especially in the vicinity of the junction between the two materials (central section).

Table 3 includes the values of the maximum principal stress obtained for the ceramic and metal that make up each of the three previous models: all-ceramic specimen, all-metal specimen, and ceramic–metal specimen models. In all three cases, it is observed that the applied load has not exceeded the yield stress of either the ceramic or the metallic material.

From the table above, it can be seen that the value of the maximum principal stress appearing in the ceramic

material in the ceramic–metal specimen model is slightly higher than that appearing in the exclusively ceramic one.

However, the stress values for the all-metal specimen are slightly lower than those for the ceramic–metal specimen.

If the residual stresses obtained for the macroscopic model had been "relocated" to the mesoscopic model prior to the application of the bending stress, in order to compare the results obtained in the monomaterial specimen, it would be sufficient to transfer the data according to a section performed on the specimen as shown in Fig. 24. For the macroscopic case, in the LA direction, the axial stresses reached values of the order of 300 MPa at the midpoint of the specimen, with a maximum value of the order of 380 MPa at a distance of 0.25 mm towards the interior of the ceramic zone and along the new axis 1. In the case of the radial stresses, the maximum value—which is around − 200 MPa—was at the midpoint, with decreasing values being obtained as one moves towards the ceramic zone and these being of a negligible order of magnitude from the 0.25 mm mentioned above.

If these values are compared with those corresponding to the bending test of the monomaterial specimen, it can be noted that in the tensile zone in the radial direction, the values calculated by the simulation could be considered roughly as the approximate "superposition" of the values of one and the other case, without, however, obtaining an acceptable comparison in the case of the compression zone. However, it is worth noting that the maximum stress values obtained in the ceramic zone in the radial direction are again located at a distance of approximately 0.2–0.3 mm from the interface, a value which is very consistent with the results of the macroscopic model. For the axial direction, the values obtained are consistent with the tensional "superposition" mentioned above.

In view of these data, it can be concluded that the ceramic material is "more loaded" by the bending stress when it is part of the ceramic–metal specimen than when it is presented alone, "taking over" part of the stresses that would "correspond" to the metal part, mainly due to the elasto-plastic behaviour of the latter.

As a fundamental difference between this case and the previous one, it is observed that when the load of $2.5 \cdot 10^5$ N is applied to the ceramic–metal specimen with the previous residual stress state, the stresses generated exceed the elastic limits of both materials, and therefore, the model abandons the elastic regime.

- Tensions in the support area.

The stresses represented by the supports have been imposed at a single point, so that the stress state that appears in these support areas reflects this singularity and, therefore,

the stress values obtained from time to time in these regions may not be very representative.

However, a higher value of the equivalent von Mises stress is observed in the support corresponding to the ceramic zone. This difference is mainly due to the shear stress, S12, which is higher in this area. As the equivalent stress is higher, plastic deformations will occur in the metal zone support, while elastic deformations are maintained in the ceramic zone. The numerical values of the equivalent stress (around 420 MPa) are sandwiched between the yield stresses of both materials, which confirms this explanation.

- Stresses in the area of load application.

As in the previous cases, specimen analyses have been carried out for a load distribution in a 1-mm zone. Therefore, the values obtained in this zone will not be taken into account. The application of the load in a narrow area (as is the extreme case of point application) causes very high stresses to appear in this region and constitutes a singularity of the stress field which does not correspond to reality, since the load is inevitably applied over an area whose dimension is at least the width of the application instrument.

- Equivalent or von Mises stress distribution.

The equivalent stress follows similar behavioural patterns to the S_{11} stress. In the tensile zone, the highest values occur in the ceramic zone. The stress field in the ceramic zone therefore reaches higher values than in the metallic zone, especially in the vicinity of the junction between the two materials (centre section).

- Stress distribution S_{11}.

The difference in materials breaks the symmetry of the distribution. In the tensile zone, the highest values (470 MPa) appear in the ceramic zone. In the metal zone, this value drops to 400 MPa, exceeding the elastic limit of the metal, which indicates that there are plastic deformations on the underside of the specimen in this zone; however, in view of the mechanical tensile strength of Nickel, which is between 450 and 600 MPa for elongations of up to 20 or 25%, the material does not break.

- Stress distribution S_{12}.

The difference in materials also breaks the symmetry of the S_{12} stress distribution, although to a lesser extent than with the S_{11} stress. The maximum values, 120 MPa, appear, as expected, in areas close to the middle fibre of the section.

The maximum principal stress appears in the lower fibres of the section and in the ceramic zone, reaching values of up to 480 MPa at a distance of 0.25 mm from the centre, which are higher than the estimated yield strength of the material. This leads to the conclusion that it is in this zone that a possible crack would initiate, should it occur. This statement is based exclusively on a stress criterion and not on criteria based on the estimation of the stress intensity factor (which, on the other hand, could not be estimated because the model does not include a crack), which makes it exclusively indicative.

The value of the maximum principal stress is very similar to that of the maximum S11 stress, since the shear stress reaches small values in the lower area of the section where cracks are expected to appear. This fact underlines that the shear stress does not contribute substantially to the initiation and subsequent propagation of cracks in this case. The area where the maximum principal stresses appear is located, in the ceramic, 0.25 mm from the central section (ceramic–metal contact).

4.3 On Residual Stresses of Thermal Origin

Regarding the residual stresses of thermal origin related to the ceramic–metal interface in the MMC, the studies carried out show that the shrinkage in the matrix is greater than the shrinkage in the reinforcement, as would be expected given the difference between the properties of one material and the other. In all cases, there is a concentration of stresses in the sharp edge of the reinforcement, which is fully compressed as a result of cooling.

As for the matrix, it is subjected to compression and tension depending on the measurement area.

As for the tensile behaviour of the MMC subjected to residual stresses, it is again observed that there is a concentration of stresses at the end of the reinforcement, reducing in magnitude, as expected, the compressive stresses corresponding to the residual stress field. The highest tensile stresses are found in the reinforcement, so that rupture will foreseeably begin in this zone and specifically at the interface of the reinforcement, which may lead to decohesion of the material.

In summary, as a consequence of the existence of prior residual stresses in the material, there will be higher compressive stresses in the reinforcement and a greater difference in the value of the stresses between the matrix and the reinforcement. Such stresses can contribute to the early appearance of defects in the material, with the reinforcement breaking and decohesion between matrix and particle as the composite plasticizes.

After the cooling process, a high residual stress concentration is observed at the sharp edges of the reinforcement. The reinforcement is compressed due to the difference between the two coefficients of thermal expansion of the constituent materials. The matrix is also compressed in the

incident zone longitudinal to the reinforcement and in the zone surrounding the fibre in the radial direction. However, the matrix is tensioned in the longitudinal direction parallel to the reinforcement and in the tangential direction around the particle.

There are many open research areas that could be studied in the future.

(a) Carry out experimental tests with the MMC in order to compare the results obtained with the FEM.

(b) Study of the mechanical behaviour of the MMC under compressive stresses, in order to find out whether the material, and more specifically different types of reinforcements, reacts in the same way to other types of stresses and to check whether the finite element method is still as effective in different cases.

(c) Carry out different tests on the material under extreme conditions of high and low temperature, checking if the behaviour of different reinforcements is the same when there are viscous creep phenomena in the matrix.

(d) Study of mechanical behaviour at high strain rates.

(e) Consider inhomogeneous temperature distributions or different cooling rates for both the ceramic–metal joints and the metal matrix and ceramic-reinforced MMC.

(f) Conduct studies for other types of MMCs (fibre-reinforced or other types of continuous reinforcement)

References

Aman S, Tomas J, Müller P, Kalman H, Rozenblat Y (2011) The investigation of breakage probability of irregularly shaped particles by impact tests. KONA Powder Particle J 29:224–235. https://doi.org/10.14356/kona.2011023

Amirkhanlou S, Ketabchi M, Parvin N, Khorsand S, Bahrami R (2013) Accumulative press bonding; a novel manufacturing process of nanostructured metal matrix composites. Mater Des 51:367–374. https://doi.org/10.1016/j.matdes.2013.04.032

Arunachalam R, PK Krishnan (2021) Compressive response of aluminum metal matrix composites. In: Encyclopedia of Materials: Composites. Elsevier Ltd., pp. 1–21. https://doi.org/10.1016/B978-0-12-803581-8.11818-1

Balokhonov R, Romanova V, Schwab E, Zemlianov A, Evtushenko E (2021) Computational microstructure-based analysis of residual stress evolution in metal-matrix composite materials during thermomechanical loading. Facta Univ Series: Mech Eng 19(2):241–252. https://doi.org/10.22190/FUME201228011B

Balokhonov R, Romanova V, Zinovieva O, Zemlianov A (2022) Microstructure-based analysis of residual stress concentration and plastic strain localization followed by fracture in metal-matrix composites. Eng Fract Mech. https://doi.org/10.1016/j.engfracmech.2021.108138

Chen JP, Gu L, He GJ (2020a). A review on conventional and nonconventional machining of SiC particle-reinforced aluminium matrix composites. Adv Manufact. Shanghai University. https://doi.org/10.1007/s40436-020-00313-2

Chen J, Chu J, Jiang W, Yao B, Zhou F, Wang Z, Zhao P (2020b) Experimental and numerical simulation to study the reduction of welding residual stress by ultrasonic impact treatment. Materials https://doi.org/10.3390/ma13040837

Chen ZY, Li GY, Wei KM, Wu LQ, Zhu YM (2021) Ultimate state and probability of particle breakage for rockfill materials based on fractal theory. Yantu Gongcheng Xuebao/Chinese J Geotech Eng 43(7):1192–1200. https://doi.org/10.11779/CJGE202107003

Das S, Chandrasekaran M, Samanta S, Kayaroganam P, Paulo Davim J (2019) Fabrication and tribological study of AA6061 hybrid metal matrix composites reinforced with SiC/B4C nanoparticles. Ind Lubr Tribol 71(1):83–93. https://doi.org/10.1108/ILT-05-2018-0166

Du W, Bai Q, Zhang B (2018) Machining characteristics of 18Ni-300 steel in additive/subtractive hybrid manufacturing. Int J Adv Manuf Technol 95(5–8):2509–2519. https://doi.org/10.1007/s00170-017-1364-0

Everaerts J, Salvati E, Uzun F, Romano Brandt L, Zhang H, Korsunsky AM (2018) Separating macro- (Type I) and micro- (Type II+III) residual stresses by ring-core FIB-DIC milling and eigenstrain modelling of a plastically bent titanium alloy bar. Acta Mater 156:43–51. https://doi.org/10.1016/j.actamat.2018.06.035

Fu H, Dönges B, Krupp U, Pietsch U, Fritzen CP, Yun X, Christ HJ (2021) Evolution of the residual stresses of types I, II, and III of duplex stainless steel during cyclic loading in high and very high cycle fatigue regimes. Int J Fatig. https://doi.org/10.1016/j.ijfatigue.2020.105972

Ge J, Ma T, Han W, Yuan T, Jin T, Fu H, Lin J (2019) Thermal-induced microstructural evolution and defect distribution of wire-arc additive manufacturing 2Cr13 part: Numerical simulation and experimental characterization. Appl Therm Eng. https://doi.org/10.1016/j.applthermaleng.2019.114335

Gigliotti M (2016) Residual thermal strains and stresses in organic matrix composite materials. J Therm Stresses 39(6):667–703. https://doi.org/10.1080/01495739.2016.1169130

González Lezcano R, Essa YE, Pérez-Castellanos JL (2003) Numerical analysis of interruption process of dynamic tensile tests using a Hopkinson bar. In Journal De Physique. IV : JP (Vol. 110, pp. 565–570). EDP Sciences. https://doi.org/10.1051/jp4:20020753

González-Lezcano RA, Del Río JM (2015) Numerical analysis of the influence of the damping rings' dimensions on interrupted dynamic tension experiment results. J Strain Anal Eng Des 50(8):594–613. https://doi.org/10.1177/0309324715601550

González-Lezcano RA, Del Río Campos JM (2019) Numerical analysis of the influence of the damping rings' thickness on interrupted dynamic tension results using SiC-reinforced ZC71 magnesium alloy specimens. Mech Sci 10(1):169–186. https://doi.org/10.5194/ms-10-169-2019

González-Lezcano RA, López-Fernández E, Cesteros-García S, Sanglier-Contreras G (2020) Influence of the fastening between thread–test samples in the stress–strain curves in tensile dynamic tests. J Braz Soc Mech Sci Eng. https://doi.org/10.1007/s40430-019-2131-y)

Han S, Zhang Z, Liu Z, Zhang H, Xue D (2020) Investigation of the microstructure and mechanical performance of bimetal components fabricated using CMT-based wire arc additive manufacturing. Mater Res Exp. https://doi.org/10.1088/2053-1591/abcb4b

Hu W, Huang Z, Wang Y, Li X, Zhai H, Zhou Y, and Chen L (2021) Layered ternary MAX phases and their MX particulate derivative reinforced metal matrix composite:a review. J Alloys Compds. Elsevier Ltd. https://doi.org/10.1016/j.jallcom.2020.157313

Huang SJ, Ali AN (2019) Experimental investigations of effects of SiC contents and severe plastic deformation on the microstructure and mechanical properties of SiCp/AZ61 magnesium metal matrix composites. J Mater Process Technol 272:28–39. https://doi.org/10.1016/j.jmatprotec.2019.05.002

Hussain A-A, Mohammed J, Al-Rasiaq AA, Al-Jaafari MAA (2017) 43 Effect of cryogenic treatments on mechanical properties of 7075 aluminum alloy matrix/Al₂O₃ particles reinforced composites. Int J Eng Res Modern Edu 525(1):2455–4200

Kalaiselvan K, Dinaharan I, and Murugan N (2021) Routes for the joining of metal matrix composite materials. In Encyclopedia of Materials: Composites (pp. 652–670). Elsevier. https://doi.org/10.1016/b978-0-12-803581-8.11899-5

Krishnan PK, Arunachalam R, Husain A, Al-Maharbi M (2021) Studies on the influence of stirrer blade design on the microstructure and mechanical properties of a novel aluminum metal matrix composite. J Manuf Sci Eng Trans ASME 143:1–13. https://doi.org/10.1115/1.4048266

Kumar S, Curtin WA (2007) Crack interaction with microstructure. Mater Today. https://doi.org/10.1016/S1369-7021(07)70207-9

Kunčická L, Macháčková A, Lavery NP, Kocich R, Cullen JCT, Hlaváč LM (2020) Effect of thermomechanical processing via rotary swaging on properties and residual stress within tungsten heavy alloy. Int J Refract Metals Hard Mater. https://doi.org/10.1016/j.ijrmhm.2019.105120

Lezcano RG, del Río J (2017) Influence of damping ring material on dynamic tensile tests. Int J Eng Technol 9(2):1107–1120. https://doi.org/10.21817/ijet/2017/v9i2/170902253

Liu S, Li Y, Chen P, Li W, Gao S, Zhang B, and Ye F (2017) Residual stresses and mechanical properties of Si3N4/SiC multilayered composites with different SiC layers. Boletin de La Sociedad Espanola de Ceramica y Vidrio. Sociedad Espanola de Ceramica y Vidrio. https://doi.org/10.1016/j.bsecv.2016.11.003

Logesh K, Bupesh Raja VK (2017) Experimental studies on impact strength of aa5052-mwcnt/ldh reinforced hybrid fibre metal laminate. Int J Mech Eng Technol 8(7):784–794

Magally K, Romero V, Arturo C, Ávila B (2016) Mathematical modeling of phase transformations and residual stress in a thermomechanical heat treatment in AISI 1045 steel by FEM. Int J Eng Res Sci 2(7):118–126

Moreno CM, Sanchez JM, Ardila LC, Molina Aldareguia JM (2009) Determination of residual stresses in cathodic arc coatings by means of the parallel beam glancing X-ray diffraction technique. Thin Solid Films 518(1):206–212. https://doi.org/10.1016/j.tsf.2009.07.011

Ong FS, Rheingans B, Goto K, Tobe H, Ohmura T, Janczak-Rusch J, Sato E (2021) Residual stress induced failure of Ti-6Al-4V/Si3N4 joints brazed with Ag-Cu-Ti filler: the effects of brazing zone's elasto-plasticity and ceramics' intrinsic properties. J Eur Ceram Soc 41(13):6319–6329. https://doi.org/10.1016/j.jeurceramsoc.2021.06.038

Patil NA, Pedapati SR, Mamat OB, Lubis HS, A. M. (2020) Effect of SiC/fly ash reinforcement on surface properties of aluminum 7075 hybrid composites. Coatings. https://doi.org/10.3390/COATINGS10060541

Ramanathan A, Krishnan PK, Muraliraja R (2019) A review on the production of metal matrix composites through stir casting—Furnace design, properties, challenges, and research opportunities. J Manuf Process. https://doi.org/10.1016/j.jmapro.2019.04.017

Sackey EK, Smith GD (2009) Empirical distribution models for slenderness and aspect ratios of core particles of particulate wood composites. Wood Fiber Sci 41(3):255–266

Salvati E, Korsunsky AM (2017) An analysis of macro-and microscale residual stresses of type I, II and III using FIB-DIC micro-ring-core milling and crystal plasticity FE modelling. Int J Plast 98:123–138. https://doi.org/10.1016/j.ijplas.2017.07.004

Senthil S, Raguraman M, and Manalan DT (2020) Manufacturing processes & recent applications of aluminium metal matrix composite materials: a review. In Materials Today: Proceedings (Vol. 45, pp. 5934–5938). Elsevier Ltd. https://doi.org/10.1016/j.matpr.2020.08.792

Shankar KV, Chandroth AM, Ghosh KJA, Sudhin CB, Pai AS, Biju A, Sriram KR (2020) Investigation of SiC particle size variation on the tribological properties of Cu-6Sn-SiC composite. Arch Foundry Eng 20(4):133–138. https://doi.org/10.24425/afe.2020.133359

Shi W, Zhang H, Zhang G, and Li Z (2006) Modifying residual stress and stress gradient in LPCVD Si3N4 film with ion implantation. Sens Actuators, A: Physical, 130–131(SPEC. ISS.), 352–357. https://doi.org/10.1016/j.sna.2005.10.008

Shin H, Park JS, Hong KS, Jung HS, Lee JK, Rhee KY (2007) Physical origin of residual thermal stresses in a multilayer ceramic capacitor. J Appl Phys. https://doi.org/10.1063/12713364

Shokrieh MM (2014) Residual stresses in composite materials. Residual stresses in composite materials (pp. 1–384). Elsevier Ltd. https://doi.org/10.1533/9780857098597

Sidhu SS, Batish A, Kumar S (2015) Analysis of residual stresses in particulate reinforced aluminium matrix composite after EDM. Mater Sci Technol (united Kingdom) 31(15):1850–1859. https://doi.org/10.1179/1743284715Y.0000000033

Sijo MT, Jayadevan KR (2016) Analysis of stir cast aluminium silicon carbide metal matrix composite: a comprehensive review. Procedia Technol 24:379–385. https://doi.org/10.1016/j.protcy.2016.05.052

Soleymani Shishvan S, Asghari AH (2017) Effects of particle shape and size distribution on particle size-dependent flow strengthening in metal matrix composites. Sci Iranica 24(3):1091–1099. https://doi.org/10.24200/sci.2017.4091

Stanković SB, Popović DM, Poparić GB (2019) Thermal properties of directionally oriented polymer fibrous materials as a function of fibre arrangement at mesoscopic level. Therm Sci 23:3117–3127. https://doi.org/10.2298/TSCI181011105S

Sun H, Zeng Y, Ye Y, Chen X, Zeng T (2020) Abnormal size effect of particle breakage probability under repeated impacts. Powder Technol 363:629–641. https://doi.org/10.1016/j.powtec.2020.01.026

Suo Y, Deng Z, Wang B, Gong Y, Jia P (2021) Constitutive model of metal matrix composites at high strain rates and its application. Mater Today Commun. https://doi.org/10.1016/j.mtcomm.2021.102328

Tavares LM, de Carvalho RM, Bonfils B, de Oliveira ALR (2020) Back-calculation of particle fracture energies using data from rotary breakage testing devices. Min Eng. https://doi.org/10.1016/j.mineng.2020.106263

Tian J, Xu P, Liu Q (2020) Effects of stress-induced solid phase transformations on residual stress in laser cladding a Fe-Mn-Si-Cr-Ni alloy coating. Mater Design. https://doi.org/10.1016/j.matdes.2020.108824

Uzi A, Levy A (2021) Energy absorption in particle breakage under impact load. Powder Technol 377:308–323. https://doi.org/10.1016/j.powtec.2020.08.061

Wady AF, Paleari AG, Queiroz TP, Margonar R, Shahdad SA, Kennedy JG, Elsanadedy HM (2003) Bond strength of repaired composites with different surface. J Prosthet Dentistry

Wang Z, Denlinger E, Michaleris P, Stoica AD, Ma D, Beese AM (2017) Residual stress mapping in Inconel 625 fabricated through additive manufacturing: method for neutron diffraction measurements to validate thermomechanical model predictions. Mater Des 113:169–177. https://doi.org/10.1016/j.matdes.2016.10.003

Wang T, Zhang J, Lee W, Ivas T, Leinenbach C (2019) Numerical analysis on the residual stress distribution and its influence factor analysis for Si3N4/42CrMo brazed joint. Simul Model Pract Theory 95:49–59. https://doi.org/10.1016/j.simpat.2019.04.007

Xiong Y, Wang W, Shi Y, Jiang R, Shan C, Liu X, Lin K (2021) Investigation on surface roughness, residual stress and fatigue property of milling in-situ TiB2/7050Al metal matrix composites. Chin J

Aeronaut 34(4):451–464. https://doi.org/10.1016/j.cja.2020.08.046

Yang C, Hu C, Xiang C, Nie H, Gu X, Xie L, He J, Zhang W, Luo J (2021) Interfacial superstructures and chemical bonding transitions at metal-ceramic interfaces. Sci Adv. https://doi.org/10.1126/SCIADV.ABF6667)

Zemlianov AV, Evtushenko EP, and Balokhonov RR (2020) Numerical simulation of deformation and fracture of metal-matrix composites with considering residual stresses. PNRPU Mech Bull 2020(4):86–96. https://doi.org/10.15593/perm.mech/2020.4.08

Zhang XX, Xiao BL, Andrä H, Ma ZY (2015) Multi-scale modeling of the macroscopic, elastic mismatch and thermal misfit stresses in metal matrix composites. Compos Struct 125:176–187. https://doi.org/10.1016/j.compstruct.2015.02.007

Zhang X, Zhang B, Mu Y, Shao S, Wick CD, Ramachandran BR, Meng WJ (2017) Mechanical failure of metal/ceramic interfacial regions under shear loading. Acta Mater 138:224–236. https://doi.org/10.1016/j.actamat.2017.07.053

Zhao Y, Jing J, Chen L, Xu F, and Hou H (2021) Current research status of interface of ceramic-metal laminated composite material for armor protection. Jinshu Xuebao/Acta Metallurgica Sinica. Chinese Academy of Sciences. https://doi.org/10.11900/0412.1961.2021.00051